

# Goal-Oriented A Posteriori Error Estimation for Compressible Fluid Flows

Ralf Hartmann<sup>1,\*</sup> and Paul Houston<sup>2,\*\*</sup>

<sup>1</sup> Institute of Applied Mathematics, University of Heidelberg, Im Neuenheimer Feld 293, D-69120 Heidelberg, Germany.

e-mail: [Ralf.Hartmann@iwr.uni-heidelberg.de](mailto:Ralf.Hartmann@iwr.uni-heidelberg.de)

<sup>2</sup> Department of Mathematics and Computer Science, University of Leicester, Leicester LE1 7RH, UK.

email: [Paul.Houston@mcs.le.ac.uk](mailto:Paul.Houston@mcs.le.ac.uk)

**Abstract.** We consider so-called ‘goal-oriented’ *a posteriori* error estimation for discontinuous Galerkin finite element approximations to the compressible Euler equations of gas dynamics. By employing a hyperbolic duality argument, we derive weighted, or Type I, *a posteriori* error estimates which bound the error measured in terms of certain target functionals of real or physical interest. The practical advantages of this general approach are illustrated by a series of numerical experiments.

## 1 Introduction

In this paper we consider the *a posteriori* error analysis and adaptive mesh design for discontinuous Galerkin finite element approximations to the compressible Euler equations of gas dynamics. In contrast to traditional *a posteriori* error estimation which seeks to control the error with respect to a given norm, here we focus on so-called ‘goal-oriented’ *a posteriori* error estimation which bounds the error measured in terms of certain target functionals of real or physical interest. Typical examples that we shall consider here include the drag and lift coefficients of a body immersed in an inviscid fluid. By employing a hyperbolic duality argument we derive a weighted, or Type I, *a posteriori* error bound which reflects the error creation and error propagation mechanisms inherent in inviscid compressible fluid flows. On the basis of this *a posteriori* estimate, we design and implement the corresponding adaptive algorithm to ensure both the reliable and efficient control of the error in the prescribed target functional. In particular, we demonstrate the superiority of the proposed approach over standard mesh refinement algorithms which employ *ad hoc* error indicators. For related work, we refer to the articles [1–3, 5], for example.

---

\* Supported by the DFG Priority Research Program and the SFB 359 at the IWR, University of Heidelberg

\*\* Paul Houston acknowledges the financial support of the EPSRC (GR/N24230).

## 2 Model problem and discretisation

We consider the two-dimensional steady state compressible Euler equations of gas dynamics. Writing  $\rho$ ,  $(u, v)$ ,  $p$  and  $E$  to denote the density, Cartesian velocity, pressure and total energy per unit mass, respectively, the equations of motion are given by

$$\operatorname{div} \mathcal{F}(\mathbf{u}) \equiv \sum_{i=1}^2 \frac{\partial}{\partial x_i} \mathbf{f}_i(\mathbf{u}) = 0 \quad \text{in } \Omega, \quad (1)$$

where  $\Omega$  is an open bounded domain in  $\mathbb{R}^2$ . Here, the vector of conservative variables  $\mathbf{u}$  and the fluxes  $\mathbf{f}_i$ ,  $i = 1, 2$ , are defined by  $\mathbf{u} = (\rho, \rho u, \rho v, \rho E)$ ,  $\mathbf{f}_1 = (\rho u, \rho u^2 + p, \rho uv, \rho H u)$  and  $\mathbf{f}_2 = (\rho v, \rho uv, \rho v^2 + p, \rho H v)$ , respectively. Additionally,  $H$  is the total enthalpy defined by  $H = E + p/\rho$ . The equation of state of an ideal gas is given by  $p = (\gamma - 1)\rho(E - (u^2 + v^2)/2)$ , where  $\gamma$  is the ratio of specific heats which, for dry air, is  $\gamma = 1.4$ .

Given that  $\Omega \subset \mathbb{R}^2$  is a bounded region, with boundary  $\Gamma$ , the system of conservation laws (1) must be supplemented by appropriate boundary conditions; for example at inflow/outflow boundaries, we require that  $A^-(\mathbf{u}, \mathbf{n})(\mathbf{u} - \mathbf{g}) = \mathbf{0}$ , where  $\mathbf{n}$  denotes the unit outward normal vector to the boundary  $\Gamma$  and  $\mathbf{g}$  is a (given) function. Here,  $A^-(\mathbf{u}, \mathbf{n})$  denotes the negative part of  $A(\mathbf{u}, \mathbf{n}) := \sum_{i=1}^2 \mathbf{n}_i \nabla_{\mathbf{u}} \mathbf{f}_i(\mathbf{u})$ .

To formulate the discontinuous Galerkin finite element method (DGFEM, for short) for (1), we first introduce some notation. Let  $\mathcal{T}_h = \{\kappa\}$  be an admissible subdivision of  $\Omega$  into open element quadrilateral domains  $\kappa$ ; here  $h$  is a piecewise constant mesh function with  $h(\mathbf{x}) = \operatorname{diam}(\kappa)$  when  $\mathbf{x}$  is in element  $\kappa$ . For  $p \in \mathbb{N}_0$ , we define the following finite element space

$$S_{h,p} = \left\{ \mathbf{v} \in [L_2(\Omega)]^4 : \mathbf{v}|_{\kappa} \in [\mathcal{Q}_p(\kappa)]^4 \quad \forall \kappa \in \mathcal{T}_h \right\},$$

where  $\mathcal{Q}_p(\kappa)$  denotes the set of tensor product polynomials of degree at most  $p$  in each coordinate direction over  $\kappa$ . Given that  $\mathbf{v} \in [H^1(\kappa)]^4$  for each  $\kappa \in \mathcal{T}_h$ , we denote by  $\mathbf{v}^+$  (resp.,  $\mathbf{v}^-$ ) the interior (resp., exterior) trace of  $\mathbf{v}$  on  $\partial\kappa$ . The DGFEM for (1) is defined as follows: find  $\mathbf{u}_h \in S_{h,p}$  such that

$$\sum_{\kappa \in \mathcal{T}_h} \left\{ - \int_{\kappa} \mathcal{F}(\mathbf{u}_h) \cdot \nabla \mathbf{v}_h \, d\mathbf{x} + \int_{\partial\kappa} \mathcal{H}(\mathbf{u}_h^+, \mathbf{u}_h^-, \mathbf{n}_{\kappa}) \mathbf{v}_h^+ \, ds + \int_{\kappa} \varepsilon \nabla \mathbf{u}_h \cdot \nabla \mathbf{v}_h \, d\mathbf{x} \right\} = 0 \quad (2)$$

for all  $\mathbf{v}_h \in S_{h,p}$ , cf. [2,4], for example. Here,  $\mathcal{H}(\cdot, \cdot, \cdot)$  denotes a *numerical flux* function, assumed to be Lipschitz continuous, consistent and conservative; in Section 4, we employ the (local) Lax–Friedrichs flux. Further,  $\varepsilon$  is an artificial viscosity defined by  $\varepsilon = C_{\varepsilon} h^{2-\beta} |\operatorname{div} \mathcal{F}(\mathbf{u}_h)|$ , where  $C_{\varepsilon}$  is a positive constant and  $0 < \beta < 1/2$ ; see [4]. For elements  $\kappa \in \mathcal{T}_h$  whose boundary intersects  $\Gamma$ , we replace  $\mathbf{u}_h^-$  by appropriate boundary/initial conditions on  $\partial\kappa \cap \Gamma$ .

### 3 A posteriori error estimation

In this section, we shall be concerned with controlling the error in the numerical solution measured in terms of a given target functional  $J(\cdot)$ . Quantities of real or physical interest include the drag and lift coefficients of a body immersed into an inviscid fluid. Writing  $S$  to denote the surface of the body and  $\bar{l}$  its chord length, these target functionals are defined by

$$J_{\text{drag}}(\mathbf{u}) = \frac{2}{\bar{l}\bar{\rho}|\bar{\mathbf{v}}|^2} \int_S (\psi_d \cdot \mathbf{n}) p \, ds, \quad J_{\text{lift}}(\mathbf{u}) = \frac{2}{\bar{l}\bar{\rho}|\bar{\mathbf{v}}|^2} \int_S (\psi_l \cdot \mathbf{n}) p \, ds,$$

respectively. Here,  $\bar{\mathbf{v}}$  and  $\bar{\rho}$  denote the reference (or free-stream) velocity and density, respectively, and

$$\psi_d = \begin{pmatrix} \cos(\alpha) & -\sin(\alpha) \\ \sin(\alpha) & \cos(\alpha) \end{pmatrix} \begin{pmatrix} 1 \\ 0 \end{pmatrix}, \quad \psi_l = \begin{pmatrix} \cos(\alpha) & -\sin(\alpha) \\ \sin(\alpha) & \cos(\alpha) \end{pmatrix} \begin{pmatrix} 0 \\ 1 \end{pmatrix},$$

where  $\alpha$  denotes the angle of attack. We note that since the pressure  $p$  is derived from the conserved variables  $(\rho, \rho u, \rho v, \rho E)$ , both target functionals  $J_{\text{drag}}(\cdot)$  and  $J_{\text{lift}}(\cdot)$  are nonlinear. Other examples of  $J(\cdot)$  include the local mean value of the field or its flux through the outflow boundary of the computational domain  $\Omega$ , and the point evaluation of a component of  $\mathbf{u}$  in  $\Omega$ .

Assuming that the functional of interest  $J(\cdot)$  is differentiable, we write  $\bar{J}(\cdot; \cdot)$  to denote the mean value linearization of  $J(\cdot)$  defined by

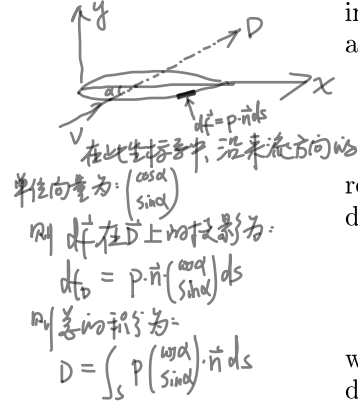
$$\bar{J}(\mathbf{u}, \mathbf{u}_h; \mathbf{u} - \mathbf{u}_h) = J(\mathbf{u}) - J(\mathbf{u}_h) = \int_0^1 J'[\theta \mathbf{u} + (1 - \theta) \mathbf{u}_h](\mathbf{u} - \mathbf{u}_h) \, d\theta, \quad (3)$$

where  $J'[\mathbf{w}](\cdot)$  denotes the Fréchet derivative of  $J(\cdot)$  evaluated at some  $\mathbf{w}$  in  $V$ . Here,  $V$  is some suitably chosen function space such that  $S_{h,p} \subset V$ . Analogously, letting  $\mathcal{N}(\mathbf{u}_h, \mathbf{v}_h)$  denote the left-hand side of (2), we write  $\mathcal{M}(\mathbf{u}, \mathbf{u}_h; \cdot, \cdot)$  to denote the mean-value linearization of  $\mathcal{N}(\cdot, \cdot)$  given by

$$\begin{aligned} \mathcal{M}(\mathbf{u}, \mathbf{u}_h; \mathbf{u} - \mathbf{u}_h, \mathbf{v}) &= \mathcal{N}(\mathbf{u}, \mathbf{v}) - \mathcal{N}(\mathbf{u}_h, \mathbf{v}) \\ &= \int_0^1 \mathcal{N}'_{\mathbf{u}}[\theta \mathbf{u} + (1 - \theta) \mathbf{u}_h](\mathbf{u} - \mathbf{u}_h, \mathbf{v}) \, d\theta \end{aligned} \quad (4)$$

for all  $\mathbf{v}$  in  $V$ . Here,  $\mathcal{N}'_{\mathbf{u}}[\mathbf{w}](\cdot, \mathbf{v})$  denotes the Fréchet derivative of  $\mathbf{u} \mapsto \mathcal{N}(\mathbf{u}, \mathbf{v})$ , for  $\mathbf{v} \in V$  fixed, at some  $\mathbf{w}$  in  $V$ . We remark that the linearization defined in (4) is only a *formal* calculation, in the sense that  $\mathcal{N}'_{\mathbf{u}}[\mathbf{w}](\cdot, \cdot)$  may not in general exist. Instead, a suitable approximation to  $\mathcal{N}'_{\mathbf{u}}[\mathbf{w}](\cdot, \cdot)$  must be determined, for example, by computing appropriate finite difference quotients of  $\mathcal{N}(\cdot, \cdot)$ , cf. [2]. For the proceeding analysis, we *assume* that the linearization (4) is well-defined. Under this hypothesis, we introduce the following *dual* problem: find  $\mathbf{z} \in V$  such that

$$\mathcal{M}(\mathbf{u}, \mathbf{u}_h; \mathbf{w}, \mathbf{z}) = \bar{J}(\mathbf{u}, \mathbf{u}_h; \mathbf{w}) \quad \forall \mathbf{w} \in V. \quad (5)$$



注意这里  $u_h \in S_{h,p}$ , 但之后需要在更richer的空间  $S_{h,p}$  内求解方程, 故应先把  $u_h$  无损地投影到  $S_{h,p}$  中去. 在高阶伴随方法中的做法体现这一点.

We assume that (5) possesses a unique solution. Clearly, the validity of this assumption depends on both the definition of  $\mathcal{M}(\mathbf{u}, \mathbf{u}_h; \cdot, \cdot)$  and the choice of the target functional under consideration, cf. [2]. For the proceeding error analysis, we must therefore *assume* that the dual problem (5) is well-posed. Under this assumption, we have the following result.

**Theorem 1.** *Let  $\mathbf{u}$  and  $\mathbf{u}_h$  denote the solutions of (1) and (2), respectively, and suppose that the dual problem (5) is well-posed. Then,*

$$J(\mathbf{u}) - J(\mathbf{u}_h) = \mathcal{E}_\Omega \equiv \sum_{\kappa \in \mathcal{T}_h} \eta_\kappa, \quad (6)$$

where

$$\eta_\kappa = \int_\kappa R_h(\mathbf{z} - \mathbf{z}_h) \, d\mathbf{x} + \int_{\partial\kappa} r_h(\mathbf{z} - \mathbf{z}_h)^+ \, ds - \int_\kappa \varepsilon \nabla \mathbf{u}_h \cdot \nabla(\mathbf{z} - \mathbf{z}_h) \, d\mathbf{x}$$

for all  $\mathbf{z}_h$  in  $S_{h,p}$ . Here,  $R_h|_\kappa = -\operatorname{div} \mathcal{F}(\mathbf{u}_h)$  and  $r_h|_\kappa = \mathcal{F}(\mathbf{u}_h) \cdot \mathbf{n}_\kappa - \mathcal{H}(\mathbf{u}_h^+, \mathbf{u}_h^-, \mathbf{n}_\kappa)$  for each  $\kappa \in \mathcal{T}_h$ .

*Proof.* Choosing  $\mathbf{w} = \mathbf{u} - \mathbf{u}_h$  in (5), recalling the linearization performed in (3), and exploiting the Galerkin orthogonality property  $\mathcal{N}(\mathbf{u}, \mathbf{v}_h) - \mathcal{N}(\mathbf{u}_h, \mathbf{v}_h) = 0$  for all  $\mathbf{v}_h$  in  $S_{h,p}$ , we get

$$\begin{aligned} J(\mathbf{u}) - J(\mathbf{u}_h) &= \bar{J}(\mathbf{u}, \mathbf{u}_h; \mathbf{u} - \mathbf{u}_h) = \mathcal{M}(\mathbf{u}, \mathbf{u}_h; \mathbf{u} - \mathbf{u}_h, \mathbf{z}) \\ &= \mathcal{M}(\mathbf{u}, \mathbf{u}_h; \mathbf{u} - \mathbf{u}_h, \mathbf{z} - \mathbf{z}_h) = -\mathcal{N}(\mathbf{u}_h, \mathbf{z} - \mathbf{z}_h) \end{aligned}$$

for all  $\mathbf{z}_h$  in  $S_{h,p}$ . Equation (6) now follows by the divergence theorem.

Based on the general error representation formula derived in Theorem 1, *a posteriori* error estimates bounding the error in the computed functional  $J(\cdot)$  may be deduced. Here, we shall confine ourselves to considering a Type I *a posteriori* error bound; it is a straightforward consequence of the error representation formula stated in the previous theorem.

**Corollary 1.** *Under the assumptions of Theorem 1, we have*

$$|J(\mathbf{u}) - J(\mathbf{u}_h)| \leq \mathcal{E}_{|\Omega|} \equiv \sum_{\kappa \in \mathcal{T}_h} |\eta_\kappa|. \quad (7)$$

*Proof.* This bound follows from (6) by application of the triangle inequality.

We end this section by noting that both the error representation formula (6) and the Type I *a posteriori* error bound (7) depend on the unknown analytical solution to the primal and dual problems. Thus, in order to render these quantities computable, both  $\mathbf{u}$  and  $\mathbf{z}$  must be replaced by suitable approximations. Here, the linearizations leading to  $\mathcal{M}(\mathbf{u}, \mathbf{u}_h; \cdot, \cdot)$  and  $\bar{J}(\mathbf{u}, \mathbf{u}_h; \cdot)$  are performed about  $\mathbf{u}_h$  and the dual solution  $\mathbf{z}$  is replaced by a DGFEM approximation  $\hat{\mathbf{z}}$  computed on the same mesh  $\mathcal{T}_h$  used for  $\mathbf{u}_h$ , but with a higher degree polynomial, i.e.,  $\hat{\mathbf{z}} \in S_{h,\hat{p}}$ ,  $\hat{p} > p$ .

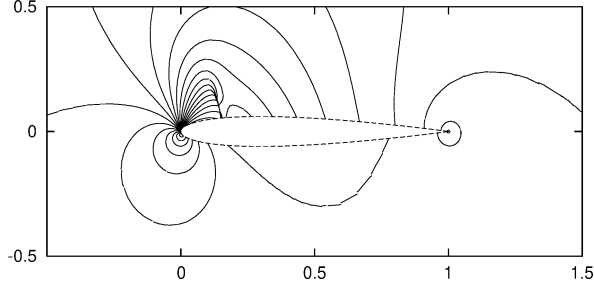


**Fig. 1.** Transonic NACA0012 flow: pressure isolines

## 4 Numerical experiments

In this section we present some numerical examples to highlight the advantages of designing an adaptive finite element algorithm based on the weighted error indicators  $|\eta_\kappa|$  in comparison with the traditional *ad hoc* error indicator  $\eta_\kappa^{\text{ad hoc}} = \|hR_h\|_{L_2(\kappa)} + \|h^{1/2}r_h\|_{L_2(\partial\kappa)}$ . Here, we employ the fixed fraction mesh refinement algorithm with refinement and derefinement fractions set to 20% and 10%, respectively; additionally, we set  $p = 1$  and  $\hat{p} = 2$ .

### 4.1 Transonic flow around a NACA0012 airfoil

In this first example, we consider the transonic flow around a NACA0012 airfoil; here, we prescribe a Mach 0.6 flow at an angle of attack  $\alpha = 5^\circ$ , with farfield density  $\rho = 1$  and pressure  $p = 1$ . The coefficient of artificial viscosity is set to  $C_\varepsilon = 0$ . The flow has a small supersonic region on the upper surface of the airfoil; as the flow slows to subsonic a small shock develops, cf. Fig. 1. Here, we consider the evaluation of the drag coefficient on the surface of the airfoil, i.e.  $J(\cdot) \equiv J_{\text{drag}}(\cdot)$ . On the basis of a fine grid computation, the reference value of the functional is given by  $J(\mathbf{u}) = 6.88 \times 10^{-3}$ .

Fig. 2 shows the meshes generated using both error indicators  $|\eta_\kappa|$  and  $\eta_\kappa^{\text{ad hoc}}$ . Given that the structure of both meshes is very similar in the sense that they are both largely concentrated in the vicinity of the leading and trailing edges of the airfoil and in the neighborhood of the shock, it is remarkable that the error in the drag coefficient is approximately 40% smaller on the mesh produced using the weighted error indicator than on the mesh (of about 30% more elements) produced by  $\eta_\kappa^{\text{ad hoc}}$ . Looking at the meshes in more detail, we see that the former mesh is less refined in the neighborhood of the shock and the trailing edge than the latter; moreover it shows an additional line of refinement upstream of the airfoil and, more prominent, along the upper and lower surfaces of the airfoil. In Fig. 3 we compare the error in the target functional using the two refinement strategies; at all refinement steps we observe the superiority of the weighted error indicators.

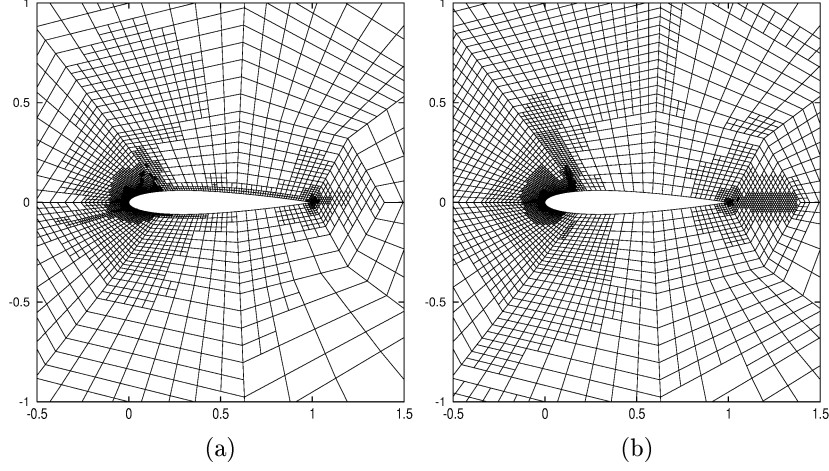


**Fig. 2.** Transonic NACA0012 flow. (a) Mesh constructed using dual error indicator with 6087 elements ( $|J(\mathbf{u}) - J(\mathbf{u}_h)| = 9.800 \times 10^{-5}$ ); (b) Mesh constructed using *ad hoc* error indicator with 7863 elements ( $|J(\mathbf{u}) - J(\mathbf{u}_h)| = 1.656 \times 10^{-4}$ )

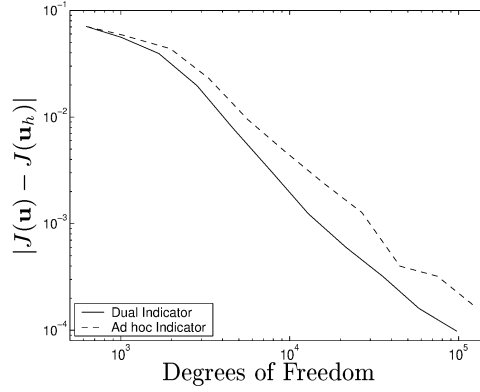


**Fig. 3.** Transonic NACA0012 flow. Convergence of  $|J(\mathbf{u}) - J(\mathbf{u}_h)|$  using the dual and *ad hoc* error indicators

In Table 1 we collect the data of the adaptive algorithm when employing the weighted indicators. Here, we show the number of elements and degrees of freedom (DOF) in  $S_{h,1}$ , the true error in the functional  $J(\mathbf{u}) - J(\mathbf{u}_h)$ , the computed error representation formula (6), the approximate *a posteriori* error bound (7) and their respective effectivity indices  $\theta_1 = \mathcal{E}_\Omega / (J(\mathbf{u}) - J(\mathbf{u}_h))$  and  $\theta_2 = \mathcal{E}_{|\Omega|} / |J(\mathbf{u}) - J(\mathbf{u}_h)|$ . First we note that on all refinement steps the correct sign of the error is predicted by the computed error representation formula  $\mathcal{E}_\Omega$ . Furthermore, whereas on very coarse meshes the quality of  $\mathcal{E}_\Omega$  is

**Table 1.** Adaptive algorithm for the transonic NACA0012 flow

Elements	DOF	$J(\mathbf{u}) - J(\mathbf{u}_h)$	$\sum_{\kappa} \eta_{\kappa}$	$\theta_1$	$\sum_{\kappa}  \eta_{\kappa} $	$\theta_2$
39	624	-7.065e-02	-2.624e-02	0.37	4.142e-02	0.59
63	1008	-5.586e-02	-1.889e-02	0.34	6.349e-02	1.14
105	1680	-3.938e-02	-1.772e-02	0.45	5.749e-02	1.46
177	2832	-1.964e-02	-1.351e-02	0.69	3.482e-02	1.77
288	4608	-7.871e-03	-6.190e-03	0.79	1.548e-02	1.97
483	7728	-3.131e-03	-2.859e-03	0.91	6.856e-03	2.19
807	12912	-1.234e-03	-1.183e-03	0.96	2.942e-03	2.38
1347	21552	-5.983e-04	-5.651e-04	0.94	1.369e-03	2.29
2226	35616	-3.193e-04	-2.916e-04	0.91	7.209e-04	2.26
3639	58224	-1.601e-04	-1.507e-04	0.94	4.062e-04	2.54
6087	97392	-9.800e-05	-9.802e-05	1.00	3.612e-04	3.69

rather poor, in the sense that  $\theta_1 = \mathcal{E}_{\Omega}/(J(u) - J(u_h))$  is noticeable smaller than one, we see that already after five refinement steps the computed error representation  $\mathcal{E}_{\Omega}$  provides remarkably sharp error estimation resulting in effectivity indices  $\theta_1 \in [0.91, 1]$ . Moreover, we observe that the Type I *a posteriori* error bound  $\mathcal{E}_{\Omega}$  is sharp, in the sense that it overestimates the true error in the computed functional by a consistent factor between 2–4.

## 4.2 Supersonic flow around a NACA0012 airfoil

In this section, we again compute the flow around a NACA0012 airfoil; here, we now consider a Mach 1.2 flow with an angle of attack  $\alpha = 5^\circ$ , and farfield density  $\rho = 1$  and pressure  $p = 1$ . The structure of the solution in this example is now quite different from Section 4.1. Here, the solution consists of a series of shocks; one located in front of the leading edge of the airfoil and one originating from the trailing edge; see Fig. 4(a) and also Fig. 6(b) which shows a mesh refined in the vicinity of the shocks.

In this example, we again consider the estimation of the drag coefficient on the surface of the airfoil; on the basis of a fine grid computation, the true value of the functional is given by  $J(\mathbf{u}) = 0.1254$ . The structure of the dual solution  $\mathbf{z}$  is shown in Fig. 4(b). Here, we see that  $\mathbf{z}$  consists of a number of singularities or ‘spikes’ which are transported along the characteristics of the linearized system. There are two thin spikes originating from the trailing edge of the airfoil which are transported upstream along the characteristics corresponding to the two eigenvalues  $\bar{v} \pm c$ , where  $\bar{v} = \sqrt{u^2 + v^2}$  denotes the velocity of the gas and  $c = \sqrt{\gamma p / \rho}$  the speed of sound. Additionally, in the

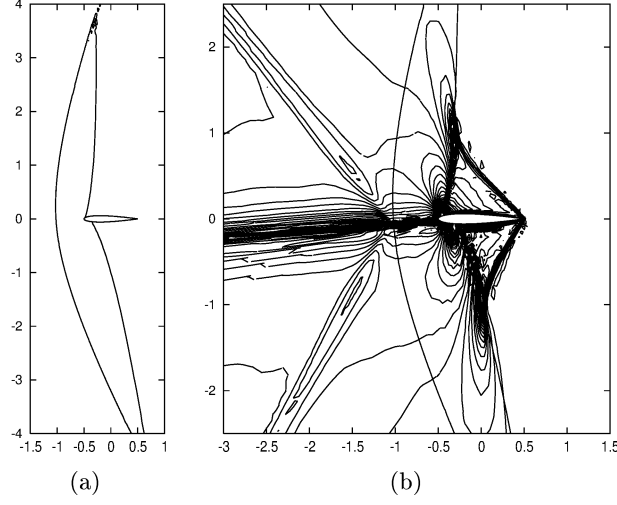


**Fig. 4.** Supersonic NACA0012 flow. (a) Mach 1 isolines of the primal solution; (b)  $z_1$  isolines of dual solution and the Mach 1 isolines of the primal solution

**Table 2.** Adaptive algorithm for the supersonic NACA0012 flow

Elements	DOF	$J(\mathbf{u}) - J(\mathbf{u}_h)$	$\sum_{\kappa} \eta_{\kappa}$	$\theta_1$	$\sum_{\kappa}  \eta_{\kappa} $	$\theta_2$
39	624	-6.735e-03	2.753e-02	-4.09	3.920e-02	5.82
60	960	-1.622e-02	-5.930e-04	0.04	3.652e-02	2.25
90	1440	-1.066e-02	-2.946e-03	0.28	3.325e-02	3.12
162	2592	-9.147e-03	-5.770e-03	0.63	2.482e-02	2.71
291	4656	-3.186e-03	-2.460e-03	0.77	1.559e-02	4.89
516	8256	-1.497e-03	-2.283e-03	1.53	1.027e-02	6.86
849	13584	-7.880e-04	-9.583e-04	1.22	6.930e-03	8.79
1428	22848	-7.275e-04	-8.209e-04	1.13	3.703e-03	5.09
2370	37920	-4.267e-04	-3.051e-04	0.71	2.767e-03	6.48
3864	61824	-2.086e-04	-2.571e-04	1.23	1.427e-03	6.84
6261	100176	-1.452e-04	-1.452e-04	1.00	8.042e-04	5.54

subsonic region of the flow, there is a singularity emanating from the leading edge of the airfoil, corresponding to mass transport along the characteristic with eigenvalue  $\bar{v}$ . As this spike crosses the first shock, it enters the supersonic region of the flow to the left of the airfoil; here, it splits into three spikes which are transported upstream along the three characteristics.



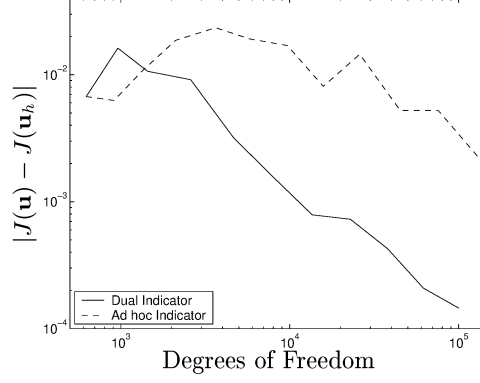


**Fig. 5.** Supersonic NACA0012 flow. Convergence of  $|J(\mathbf{u}) - J(\mathbf{u}_h)|$  using the dual and *ad hoc* error indicators

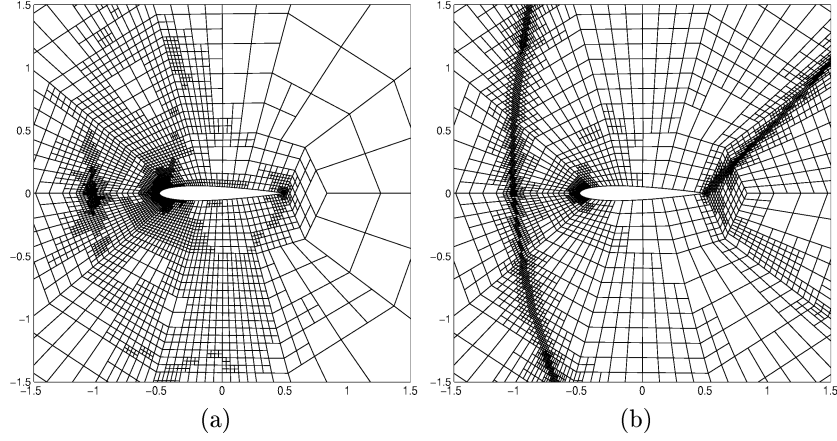


**Fig. 6.** Supersonic NACA0012 flow. (a) Mesh constructed using dual error indicator with 6261 elements ( $|J(\mathbf{u}) - J(\mathbf{u}_h)| = 1.452 \times 10^{-4}$ ); (b) Mesh constructed using *ad hoc* error indicator with 14037 elements ( $|J(\mathbf{u}) - J(\mathbf{u}_h)| = 5.669 \times 10^{-3}$ )

In Table 2 we show the performance of our adaptive algorithm with  $C_\varepsilon = 1/20$  and  $\beta = 1/10$ . Here, we see after the first few refinement steps, the quality of the computed error representation formula  $\mathcal{E}_\Omega$  is extremely good, with  $\theta_1 \in (0.71, 1.53)$ . Moreover, we observe that the Type I *a posteriori* estimate provides a reliable upper bound on the size of the error in the computed functional  $J(\cdot)$ . As in the previous example, we see that the adaptively refined meshes generated by employing  $|\eta_\kappa|$  are much more economical than those produced using  $\eta_\kappa^{\text{ad hoc}}$ . Indeed, in Fig. 5 we clearly observe the superiority of the former error indicator; on the final mesh the true error in the computed drag is over an order of magnitude smaller when  $|\eta_\kappa|$  is employed.

Finally, in Fig. 6 we show the meshes produced using both error indicators. Here, we see that the mesh constructed using  $\eta_{\kappa}^{\text{ad hoc}}$  is concentrated in the neighbourhood of the two shocks. In contrast, the mesh produced using the weighted error indicator  $|\eta_{\kappa}|$  is mainly refined at leading- and trailing-edges of the airfoil, as well as in the region of the first shock where the spike of the dual solution crosses from the subsonic to supersonic regions of the flow. The other parts of this shock as well as the shock emanating from the trailing edge of the airfoil are not resolved. This indicates that a good numerical resolution of the shocks everywhere in the computational domain is irrelevant for the accurate approximation of the drag coefficient in this example.

## 5 Concluding remarks

In this paper we have considered the derivation of ‘goal-oriented’ *a posteriori* estimates for inviscid compressible fluid flows which bound the error measured in terms of certain target functionals of real or physical interest. These error bounds stem from employing a hyperbolic duality argument together with the Galerkin orthogonality of the finite element method. On the basis of this *a posteriori* estimate, we have designed and implemented the corresponding adaptive algorithm to ensure both the reliable and efficient control of the error in the prescribed target functional. Numerical experiments highlighting the flexibility of this approach have been presented.

### Acknowledgement

Part of this work was performed using the University of Leicester Mathematical Modelling Centre’s supercomputer which was purchased through the EPSRC strategic equipment initiative.

## References

1. R. BECKER AND R. RANNACHER, *A feed-back approach to error control in finite element methods: Basic analysis and examples*. East-West J. Num. Math., 4:237–264, 1996.
2. R. HARTMANN AND P. HOUSTON, *Adaptive Discontinuous Galerkin Finite Element Methods for Nonlinear Hyperbolic Conservation Laws*. Leicester University Technical Report 2001/20, 2001. (Submitted for publication).
3. P. HOUSTON, R. RANNACHER AND E. SÜLI, *A posteriori error analysis for stabilised finite element approximations of transport problems*. Comput. Meth. Appl. Mech. Engrg. 190(11-12):1483–1508, 2000.
4. J. JAFFRE, C. JOHNSON AND A. SZEPESSY, *Convergence of the discontinuous Galerkin finite element method for hyperbolic conservation laws*. Math. Models Methods Appl. Sci. 5(3):367–386, 1995.
5. M.G. LARSON AND T.J. BARTH, *A posteriori error estimation for discontinuous Galerkin approximations of hyperbolic systems*. In: B. Cockburn, G. Karniadakis, and C.-W. Shu, editors, *Discontinuous Galerkin Finite Element Methods*. Lecture Notes in Computational Science and Engineering, Volume 11. Springer-Verlag 2000.